

**The following resources related to this article are available online at [www.sciencemag.org](http://www.sciencemag.org) (this information is current as of July 25, 2009 ):**

**Updated information and services**, including high-resolution figures, can be found in the online version of this article at:

<http://www.sciencemag.org/cgi/content/full/325/5938/294>

**Supporting Online Material** can be found at:

<http://www.sciencemag.org/cgi/content/full/325/5938/294/DC1>

A list of selected additional articles on the Science Web sites **related to this article** can be found at:

<http://www.sciencemag.org/cgi/content/full/325/5938/294#related-content>

This article **cites 10 articles**, 2 of which can be accessed for free:

<http://www.sciencemag.org/cgi/content/full/325/5938/294#otherarticles>

This article has been **cited by** 1 articles hosted by HighWire Press; see:

<http://www.sciencemag.org/cgi/content/full/325/5938/294#otherarticles>

This article appears in the following **subject collections**:

Physics

<http://www.sciencemag.org/cgi/collection/physics>

Information about obtaining **reprints** of this article or about obtaining **permission to reproduce this article** in whole or in part can be found at:

<http://www.sciencemag.org/about/permissions.dtl>

virus, for which there may be varying degrees of homotypic and heterotypic immunity (32). Secondary infections may occur only when individuals encounter a strain that substantially differs from the one causing primary infection. Furthermore, the true effect of vaccination may differ slightly from that suggested by our model. If vaccination conferred highly protective immunity comparable to that exhibited after two natural infections, our model suggests that the level of herd immunity generated by vaccination could lead to the elimination of the infection from the population at very high coverage levels (10). However, one cannot rule out the possible emergence of new rotavirus strains in response to vaccine pressure, and information on rotavirus genetic diversity will be crucial to understand the long-term effectiveness of any immunization program.

We can extend our U.S.-based analysis to the context of developing countries, where rotavirus remains a substantial cause of childhood morbidity and mortality and disease dynamics differ. The high birth rates typical of developing countries may help explain why rotavirus exhibits less seasonal variation in such settings (33), although climatic factors could also play a role. In addition, rotavirus vaccine efficacy remains somewhat unclear in developing country settings and could be lower than in the United States because of several factors that might interfere with vaccine performance (e.g., presence of maternal antibodies, high levels of coinfection with other enteropathogens, higher rates of malnutrition, and greater prevalence of uncommon rotavirus strains). Efficacy trials of rotavirus vaccines are ongoing in several countries of Asia and Africa, and results are expected in the next 6 to 12 months. Differences in population demographics,

epidemiology of rotavirus disease, and, potentially, vaccine effectiveness, would need to be carefully considered when predicting the benefits of vaccination in developing countries, and the vaccine experience of industrialized nations may not directly translate to countries with high rotavirus mortality burden. Introducing vaccination would likely decrease the overall burden of disease but could have important dynamic consequences, which are key to explore in future research.

#### References and Notes

1. A. Z. Kapikian, R. M. Chanock, in *Fields Virology*, B. N. Fields *et al.*, Eds. (Lippincott-Raven, Philadelphia, 2001), vol. 2, pp. 1657–1708.
2. U. D. Parashar, C. J. Gibson, J. S. Bresse, R. I. Glass, *Emerg. Infect. Dis.* **12**, 304 (2006).
3. U. D. Parashar, E. G. Hummelman, J. S. Bresse, M. A. Miller, R. I. Glass, *Emerg. Infect. Dis.* **9**, 565 (2003).
4. T. K. Fischer *et al.*, *J. Infect. Dis.* **195**, 1117 (2007).
5. R. I. Glass, U. D. Parashar, *N. Engl. J. Med.* **354**, 75 (2006).
6. R. I. Glass *et al.*, *Lancet* **368**, 323 (2006).
7. G. M. Ruiz-Palacios *et al.*, *N. Engl. J. Med.* **354**, 11 (2006).
8. T. Vesikari *et al.*, *N. Engl. J. Med.* **354**, 23 (2006).
9. A. C. Linhares *et al.*, *Lancet* **371**, 1181 (2008).
10. Materials and methods are available as supporting material on Science Online.
11. C. W. LeBaron, J. Lew, R. I. Glass, J. M. Weber, G. M. Ruiz-Palacios, *JAMA* **264**, 983 (1990).
12. T. J. Torok *et al.*, *Pediatr. Infect. Dis. J.* **16**, 941 (1997).
13. R. M. Turtios *et al.*, *Pediatr. Infect. Dis. J.* **25**, 451 (2006).
14. C. Viboud *et al.*, *Science* **312**, 447 (2006); published online 29 March 2006 (10.1126/science.1125237).
15. Y. Xia, O. N. Bjornstad, B. T. Grenfell, *Am. Nat.* **164**, 267 (2004).
16. M. I. Nelson, L. Simonsen, C. Viboud, M. A. Miller, E. C. Holmes, *PLoS Pathog.* **3**, 1220 (2007).
17. M. J. Cox, G. F. Medley, *Epidemiol. Infect.* **131**, 719 (2003).
18. H. Nakajima *et al.*, *Lancet* **357**, 1950 (2001).
19. S. Arista *et al.*, *J. Virol.* **80**, 10724 (2006).
20. S. G. Purohit, S. D. Kelkar, V. Simha, *J. Diarrhoeal Dis. Res.* **16**, 74 (1998).
21. B. T. Grenfell, O. N. Bjornstad, J. Kappey, *Nature* **414**, 716 (2001).
22. A. J. Conlan, B. T. Grenfell, *Proc. R. Soc. London Ser. B* **274**, 1133 (2007).
23. G. Cilla, E. Perez-Trallero, M. C. Lopez-Lopategui, A. Gilsetas, M. Gomariz, *Epidemiol. Infect.* **125**, 677 (2000).
24. B. E. Hamilton, P. D. Sutton, S. J. Ventura, "Revised birth and fertility rates for the 1990s and new rates for Hispanic populations, 2000 and 2001: United States" (National Center for Health Statistics, 2003).
25. Centers for Disease Control and Prevention National Center for Health Statistics, VitalStats, [www.cdc.gov/nchs/vitalstats/VitalStatsbirths.htm](http://www.cdc.gov/nchs/vitalstats/VitalStatsbirths.htm) [accessed 22 April 2008].
26. Agency for Healthcare Quality and Research (AHRQ), [www.hcup-us.ahrq.gov/databases.jsp](http://www.hcup-us.ahrq.gov/databases.jsp).
27. M. A. Staat *et al.*, *MMWR Morb. Mortal. Wkly. Rep.* **57**, 697 (2008).
28. R. M. Anderson, R. M. May, *Infectious Diseases of Humans: Dynamics and Control* (Oxford Univ. Press, Oxford, 1991).
29. D. I. Bernstein, D. S. Sander, V. E. Smith, G. M. Schiff, R. L. Ward, *J. Infect. Dis.* **164**, 277 (1991).
30. D. L. Smith, B. Lucey, L. A. Waller, J. E. Childs, L. A. Real, *Proc. Natl. Acad. Sci. U.S.A.* **99**, 3668 (2002).
31. D. A. Cummings *et al.*, *Nature* **427**, 344 (2004).
32. B. Jiang, J. R. Gentsch, R. I. Glass, *Clin. Infect. Dis.* **34**, 1351 (2002).
33. S. M. Cook, R. I. Glass, C. W. LeBaron, M. S. Ho, *Bull. World Health Organ.* **68**, 171 (1990).
34. V.E.P. and B.G. were supported by NIH (grant R01 GM083983-01) and the Bill and Melinda Gates Foundation. V.E.P., B.G., and L.S. were also supported by the RAPIDD program of the Science and Technology Directorate, U.S. Department of Homeland Security, and the Fogarty International Center, NIH. The findings and conclusions in this report are those of the authors and do not necessarily represent the views of the Centers for Disease Control and Prevention (CDC).

#### Supporting Online Material

[www.sciencemag.org/cgi/content/full/325/5938/290/DC1](http://www.sciencemag.org/cgi/content/full/325/5938/290/DC1)

Materials and Methods  
Figs. S1 to S12  
Tables S1 to S4  
References

16 February 2009; accepted 3 June 2009  
10.1126/science.1172330

## Nonlocal Transport in the Quantum Spin Hall State

Andreas Roth,<sup>1</sup> Christoph Brüne,<sup>1</sup> Hartmut Buhmann,<sup>1</sup> Laurens W. Molenkamp,<sup>1\*</sup> Joseph Maciejko,<sup>2,3</sup> Xiao-Liang Qi,<sup>2,3</sup> Shou-Cheng Zhang<sup>2,3</sup>

Nonlocal transport through edge channels holds great promise for low-power information processing. However, edge channels have so far only been demonstrated to occur in the quantum Hall regime, at high magnetic fields. We found that mercury telluride quantum wells in the quantum spin Hall regime exhibit nonlocal edge channel transport at zero external magnetic field. The data confirm that the quantum transport through the (helical) edge channels is dissipationless and that the contacts lead to equilibration between the counterpropagating spin states at the edge. The experimental data agree quantitatively with the theory of the quantum spin Hall effect. The edge channel transport paves the way for a new generation of spintronic devices for low-power information processing.

The search for topological states of quantum matter has become an important goal in condensed matter physics. Inside a topological insulator, the conventional laws of electrodynamics are substantially altered (1), which may have applications in constructing novel devices for the processing of (quantum) information. The

quantum spin Hall (QSH) state (2, 3) is a topologically nontrivial state of matter that exists in the absence of any external magnetic field. It has a bulk energy gap but gapless helical edge states protected by time reversal symmetry. In the QSH regime, opposite spin states forming a Kramers doublet counterpropagate at the edge (4, 5). Re-

cently, the QSH state was theoretically predicted in HgTe quantum wells (6). There is a topological quantum phase transition at a critical thickness  $d_c$  of the quantum well, separating the trivial insulator state for  $d < d_c$  from the QSH insulator state for  $d > d_c$ . Soon after the theoretical prediction, evidence for the QSH state was observed in transport measurements (7). In the QSH regime, experiments measured a conductance  $G$  close to twice the quantum unit of conductance  $G = 2e^2/h$  (where  $e$  is the charge on the electron and  $h$  is Planck's constant); this value is consistent with quantum transport due to helical edge states. However, such a conductance quantization in small Hall bar geometries does not allow us to distinguish experimentally between ballistic and edge channel transport in a convincing manner. Thus, it is important to be able to prove experi-

<sup>1</sup>Physikalisches Institut (EP3) and Röntgen Center for Complex Material Systems, Universität Würzburg, Am Hubland, 97074 Würzburg, Germany. <sup>2</sup>Department of Physics, Stanford University, Stanford, CA 94305, USA. <sup>3</sup>Stanford Institute for Materials and Energy Sciences, SLAC National Accelerator Laboratory, 2575 Sand Hill Road, Menlo Park, CA 94025, USA.

\*To whom correspondence should be addressed. E-mail: molenkmp@physik.uni-wuerzburg.de

mentally in an unambiguous manner the existence of edge channels in HgTe quantum wells.

**Ohm's law versus nonlocal transport.** In conventional diffusive electronics, bulk transport satisfies Ohm's law. The resistance is proportional to the length and inversely proportional to the cross-sectional area, implying the existence of a local

resistivity or conductivity tensor. However, the existence of edge states necessarily leads to nonlocal transport, which invalidates the concept of local resistivity. Such nonlocal transport has been experimentally observed in the quantum Hall (QH) regime in the presence of a large magnetic field (8), and the nonlocal transport is well described by a quantum

transport theory based on the Landauer-Büttiker formalism (9). These measurements constitute definitive experimental evidence for the existence of edge states in the QH regime.

We report nonlocal transport measurements in HgTe quantum wells that demonstrate the existence of the predicted extended edge channels. We have fabricated structures more complicated than a standard Hall bar that allow a detailed investigation of the transport mechanism. In addition, we present the theory of quantum transport in the QSH regime, and uncover the effects of macroscopic time irreversibility on the helical edge states.

**Device structure.** We present experimental results on four different devices. The behavior in these structures is exemplary for the  $\sim 50$  devices we studied. The devices were fabricated from HgTe/(Hg,Cd)Te quantum well structures with well thicknesses of  $d = 7.5$  nm (samples D1, D2, and D3) and 9.0 nm (sample D4). Note that all wells have a thickness  $d > d_c \approx 6.3$  nm, and thus exhibit the topologically nontrivial inverted band structure. At zero gate voltage, the samples are n-type and have a carrier density of  $n_s \approx 3 \times 10^{11} \text{ cm}^{-2}$  and a mobility of  $1.5 \times 10^5 \text{ cm}^2 \text{ V}^{-1} \text{ s}^{-1}$ , with small variations between the different wafers. The devices are lithographically patterned using electron-beam lithography and subsequent Ar ion-beam etching. Devices D1 and D2 are micrometer-scale Hall bars with exact dimensions as indicated in the insets of Fig. 1. Devices D3 and D4 are dedicated structures for identifying nonlocal transport, with schematic structure given in Fig. 2. All devices are fitted with a 110-nm-thick  $\text{Si}_3\text{N}_4/\text{SiO}_2$  multi-layer gate insulator and a Ti (5 nm)–Au (50 nm) gate electrode stack.

By applying a voltage  $V_g$  to the top gate, the electron carrier density of the quantum well can be adjusted, going from an n-type behavior at positive gate voltages through the bulk insulator state into a p-type regime at negative gate voltages. For reasons of comparison, the experimental data in Figs. 1, 3, and 4 are plotted as a function of a normalized gate voltage  $V^* = V_g - V_{\text{thr}}$  ( $V_{\text{thr}}$  is defined as the voltage for which the resistance

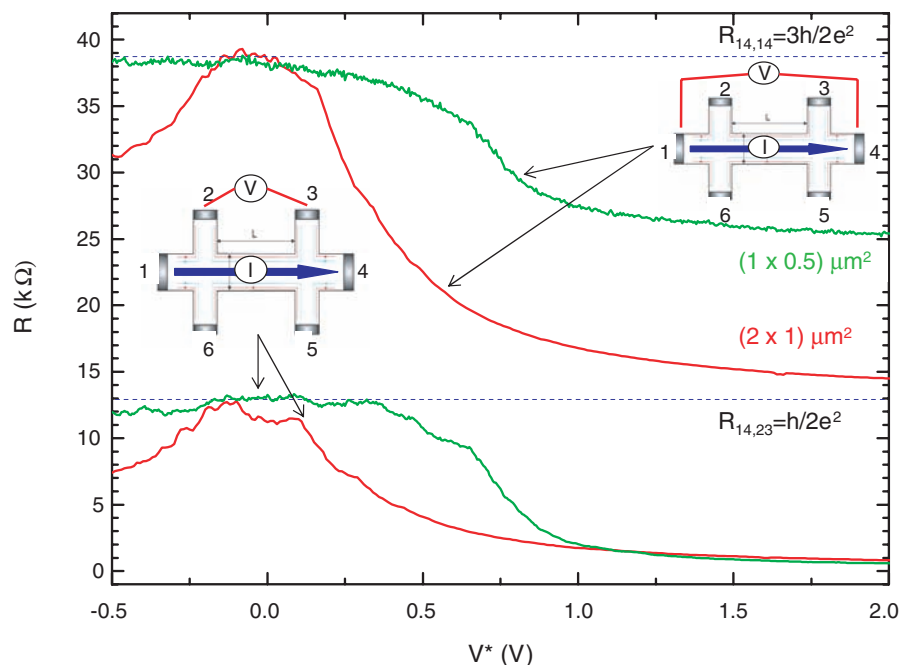


**Fig. 1.** Two-terminal ( $R_{14,14}$ ) (top two traces) and four-terminal ( $R_{14,23}$ ) (bottom traces) resistance versus (normalized) gate voltage for the Hall bar devices D1 and D2 with dimensions (length  $\times$  width) as indicated. The dotted blue lines indicate the resistance values expected from the Landauer-Büttiker approach.

**Fig. 2.** Schematic layout of devices D3 (A) and D4 (B). The gray areas are the mesas, the yellow areas the gates, with dimensions as indicated. The numbers indicate the coding of the leads.

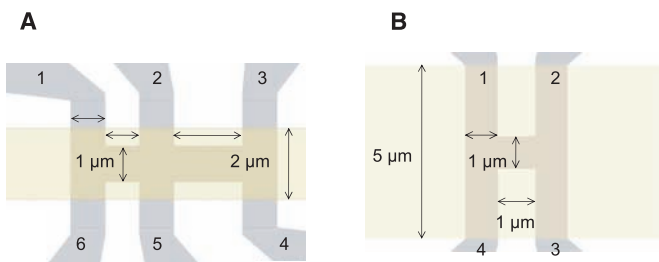
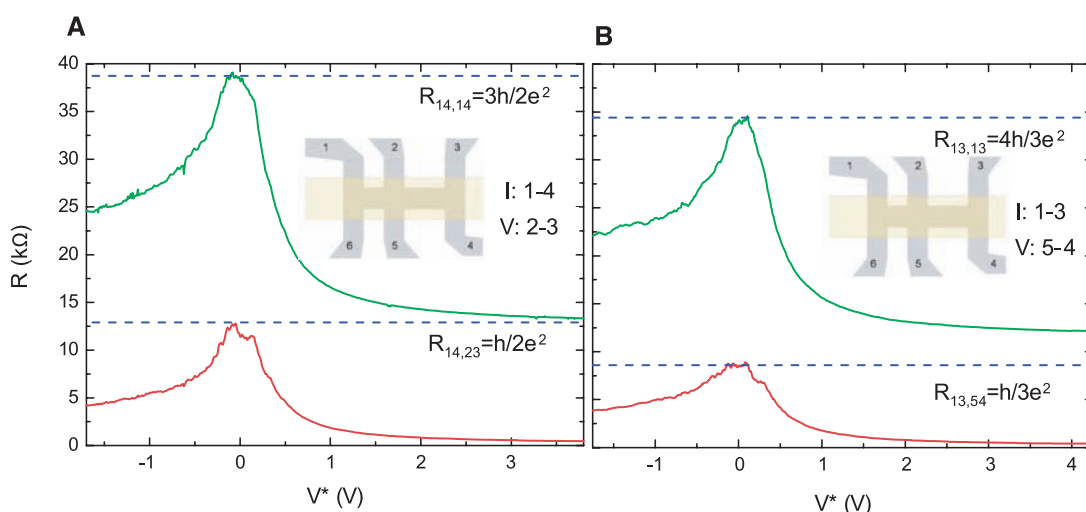


**Fig. 3.** Four- and two-terminal resistance measured on device D3: (A)  $R_{14,23}$  (red line) and  $R_{14,14}$  (green line) and (B)  $R_{13,54}$  (red line) and  $R_{13,13}$  (green line). The dotted blue lines indicate the expected resistance value from a Landauer-Büttiker calculation.



is largest). Measurements were performed at a lattice temperature of 10 mK for samples D1, D2, and D3 and at 1.8 K for sample D4, using low-frequency (13 Hz) lock-in techniques under voltage bias. The four-terminal resistance (Fig. 1) shows a maximum at about  $h/2e^2$ , in agreement with the results of (7). The contact resistance should be insensitive to the gate voltage and can be measured from the resistance deep in the metallic region. By subtracting the contact resistance, we find that the two-terminal resistance has its maximum at about  $3h/2e^2$  (Fig. 1). This value is exactly what is expected from the theory of QSH edge transport obtained from the Landauer-Büttiker formula.

**Transport on the edge.** Within the general Landauer-Büttiker formalism (10), the current-voltage relationship is expressed as

$$I_i = \frac{e^2}{h} \sum_j (T_{ji} V_i - T_{ij} V_j) \quad (1)$$

where  $I_i$  is the current flowing out of the  $i$ th electrode into the sample region,  $V_i$  is the voltage on the  $i$ th electrode, and  $T_{ji}$  is the transmission probability from the  $i$ th to the  $j$ th electrode. The total current is conserved in the sense that  $\sum_i I_i = 0$ . A voltage lead  $j$  is defined by the condition that it draws no net current (i.e.,  $I_j = 0$ ). The physical currents are left invariant if the voltages on all electrodes are shifted by a constant amount  $\mu$ , implying that  $\sum_i T_{ij} = \sum_i T_{ji}$ . In a time reversal-invariant system, the transmission coefficients satisfy the condition  $T_{ij} = T_{ji}$ .

For a general two-dimensional sample, the number of transmission channels scales with the width of the sample, so that the transmission matrix  $T_{ij}$  is complicated and nonuniversal. However, a tremendous simplification arises if the quantum transport is entirely dominated by the edge states. In the QH regime, chiral edge states are responsible for the transport. For a standard Hall bar with  $N$  current and voltage leads attached (compare the insets of Fig. 1 with  $N = 6$ ), the transmission matrix elements for the  $\nu = 1$  QH state are given by  $T(\text{QH})_{i+1,i} = 1$ , for  $i = 1, \dots, N$ , and all other matrix elements vanish identically. Here we periodically identify the  $i = N + 1$  electrode with  $i = 1$ . Chiral edge states are protected from backscattering; therefore, the  $i$ th electrode transmits perfectly to the neighboring  $(i + 1)$ th electrode on one side only. In the example of current leads on electrodes

1 and 4, and voltage leads on electrodes 2, 3, 5, and 6, one finds that  $I_1 = -I_4 \equiv I_{14}$ ,  $V_2 - V_3 = 0$ , and  $V_1 - V_4 = (h/e^2)I_{14}$ , giving a four-terminal resistance of  $R_{14,23} = 0$  and a two-terminal resistance of  $R_{14,14} = h/e^2$ .

In the case of helical edge states in the QSH regime, opposite spin states form a Kramers pair, counterpropagating on the same edge. The helical edge states are protected from backscattering due to time reversal symmetry, and the transmission from one electrode to the next is perfect. From this point of view, the helical edge states can be viewed as two copies of chiral edge states related by time reversal symmetry. Therefore, the transmission matrix is given by  $T(\text{QSH}) = T(\text{QH}) + T^*(\text{QH})$ , implying that the only nonvanishing matrix elements are given by

$$T(\text{QSH})_{i+1,i} = T(\text{QSH})_{i,i+1} = 1 \quad (2)$$

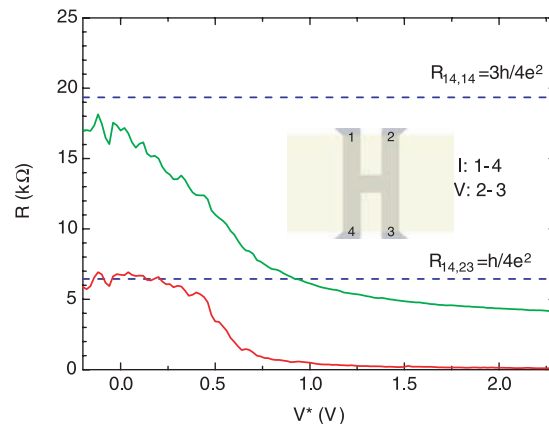
Considering again the example of current leads on electrodes 1 and 4 and voltage leads on electrodes 2, 3, 5, and 6, one finds that  $I_1 = -I_4 \equiv I_{14}$ ,  $V_2 - V_3 = (h/2e^2)I_{14}$ , and  $V_1 - V_4 = (3h/e^2)I_{14}$ , giving a four-terminal resistance of  $R_{14,23} = h/2e^2$  and a two-terminal resistance of  $R_{14,14} = 3h/2e^2$ . The experimental data in Fig. 1 confirm this picture. For both micro-Hall bar structures D1 and D2 that differ only in the dimensions of the area between voltage contacts 3 and 4, we observe exactly the expected resistance values for  $R_{14,23} = h/2e^2$  and  $R_{14,14} = 3h/2e^2$  for gate voltages where the samples are in the QSH regime.

**Dissipationless transport.** Conceptually, one might sense a paradox between the dissipationless nature of the QSH edge states and the finite four-terminal longitudinal resistance  $R_{14,23}$ , which vanishes for the QH state. We can generally assume that the microscopic Hamiltonian governing the voltage leads is invariant under time reversal symmetry; therefore, one would naturally ask how such leads could cause the dissipation of the helical edge states, which are protected by time reversal symmetry. In nature, the time reversal symmetry can be broken in two ways: at the level of the microscopic Hamiltonian, or at the level of the macroscopic irreversibility in systems whose microscopic Hamiltonian respects the time reversal symmetry. When the helical edge

states propagate without dissipation inside the QSH insulator between the electrodes, neither form of time reversal symmetry breaking is present. As a result, the two counterpropagating channels can be maintained at two different quasi-chemical potentials, leading to a net current flow. However, once they enter the voltage leads, they interact with a reservoir containing infinitely many low-energy degrees of freedom, and the time reversal symmetry is effectively broken by the macroscopic irreversibility. As a result, the two counterpropagating channels equilibrate at the same chemical potential, determined by the voltage of the lead. Dissipation occurs with the equilibration process. The transport Eq. 1 breaks the macroscopic time reversal symmetry, even though the microscopic time reversal symmetry is ensured by the relationship  $T_{ij} = T_{ji}$ . In contrast to the case of QH state, the absence of dissipation of the QSH helical edge states is protected by Kramers' theorem, which relies on the quantum phase coherence of wave functions. Thus, dissipation can occur once the phase coherence is destroyed in the metallic leads. By contrast, the robustness of QH chiral edge states does not require phase coherence. The result of a more rigorous and microscopic analysis on the different role played by a metallic lead in QH and QSH states (11) agrees with the simple transport Eqs. 1 and 2. These two equations, which correctly describe the dissipationless quantum transport inside the QSH insulator and the dissipation inside the electrodes, can be subjected to more stringent experimental tests than the two- and four-terminal experiments of Fig. 1 by considering devices D3 and D4 (Fig. 2).

**Helical versus chiral.** A further difference between helical and chiral edge channels is evident from our experiments on the six-terminal device D3 (Fig. 3). When the longitudinal resistance of device D3 is measured by passing a current through contacts 1 and 4 and by detecting the voltage between contacts 2 and 3 ( $R_{14,23}$ ), we find, similar to the results of Fig. 1, a resistance value of  $h/2e^2$  when the bulk of the device is gated into the insulating regime (Fig. 3A). However, the longitudinal resistance is markedly different in a slightly modified configuration, where the current is passed through contacts 1 and 3 and the voltage is measured between contacts 5 and 4 ( $R_{13,54}$ ) (Fig. 3B). We now find  $R_{13,54} \approx 8.6$  kilohms, which is markedly different from what one would expect for either the QH transport or the purely diffusive transport, where this configuration would be equivalent to the previous one. Application of Eqs. 1 and 2 actually predicts that the observed behavior is indeed what one expects for helical edge channels. This resistance value can again be expressed as an integer fraction of the inverse conductance quanta  $e^2/h$ :  $R_{13,54} = h/3e^2$ . This result shows that the current through the device is influenced by the number of ohmic contacts in the current path. These ohmic contacts lead to the equilibration of the chemical potentials between the two counterpropagating helical edge channels inside the contact. There are also some devices for which

**Fig. 4.** Nonlocal four-terminal resistance and two-terminal resistance measured on the H-bar device D4:  $R_{14,23}$  (red line) and  $R_{14,14}$  (green line). Again, the dotted blue line represents the theoretically expected resistance value.



the maximal resistance does not match the theoretical value obtained from Eqs. 1 and 2, but still remains an integer fraction of the quantum  $h/e^2$ . This result can be naturally understood as due to inhomogeneities in the gate action (e.g., due to interface trap states) inducing some metallic droplets close to the edge channels while the bulk of the sample is insulating. A metallic droplet can cause dephasing of the electronic wave function, leading to fluctuations in the device resistance. For full dephasing, the droplet plays the role of an additional ohmic contact, just as for the chiral edge channels in the QH regime (8). More details on the effects of additional ohmic contacts in the QSH state are given in (11).

Another measurement that directly confirms the nonlocal character of the helical edge channel transport in the QSH regime is in Fig. 4, which shows data obtained from device D4, in the shape of the letter H. In this four-terminal device, the current is passed through contacts 1 and 4 and the voltage is measured between contacts 2 and 3. In the metallic n-type regime (low gate voltage), the voltage signal tends to zero. In the insulating regime, however, the nonlocal resistance signal increases to  $\sim 6.5$  kilohms, which again fits perfectly to the result of Landauer-Büttiker considerations:  $R_{14,23} = h/4e^2 \approx 6.45$  kilohms. Classically, one would expect only a minimal signal in this configuration (from Poisson's equation, assuming diffusive transport, one estimates a signal of about 40 ohms), and certainly not one that increases so strongly when the bulk of the sample is depleted. This signal measured here is fully nonlocal and can be taken (as was done 20 years ago for the QH regime) as definite evidence of the existence of edge channel transport in the QSH regime. A similar nonlocal voltage has been studied in a metallic spin

Hall system with the same H-bar geometry (12), in which case the nonlocal voltage can be understood as a combination of the spin Hall effect and the inverse spin Hall effect (13). The quantized nonlocal resistance  $h/4e^2$  we find here is the quantum counterpart of the metallic case. For example, if we assume that the chemical potential in contact 1 is higher than that in contact 4 (compare to the layout of D4 in Fig. 2B), more electrons will be injected into the upper edge state in the horizontal segment of the H-bar than into the lower edge state. Because on opposite edges the right-propagating edge states have opposite spin, this implies that a spin-polarized current is generated by an applied bias  $V_1 - V_4$ , comparable to a spin Hall effect. When this spin-polarized current is injected into the right leg of the device, the inverse effect occurs. Electrons in the upper edge flow to contact 2 while those in the lower edge flow to contact 3, establishing a voltage difference between those two contacts due to the charge imbalance between the edges. The right leg of the device thus acts as a detector for the injected spin-polarized current, which corresponds to the inverse spin Hall effect.

**Concluding remarks.** The multiterminal and nonlocal transport experiments on HgTe microstructures in the QSH regime demonstrate that charge transport occurs through extended helical edge channels. We have extended the Landauer-Büttiker model for multiterminal transport in the QH regime to the case of helical QSH edge channels and have shown that this model convincingly explains the observations. Logic devices based on the complementary metal oxide semiconductor design generate considerable heating due to the ohmic dissipation within the channel. Our work on conductance quantization demonstrates that electrons can be transported coherently

within the edge channel without ohmic dissipation. Such an effect can be used to construct logic devices with improved performance.

#### References and Notes

1. S. C. Zhang, *Physics* **1**, 6 (2008).
2. C. L. Kane, E. J. Mele, *Phys. Rev. Lett.* **95**, 226801 (2005).
3. B. A. Bernevig, S. C. Zhang, *Phys. Rev. Lett.* **96**, 106802 (2006).
4. C. Wu, B. A. Bernevig, S. C. Zhang, *Phys. Rev. Lett.* **96**, 106401 (2006).
5. C. Xu, J. Moore, *Phys. Rev. B* **73**, 045322 (2006).
6. B. A. Bernevig, T. L. Hughes, S.-C. Zhang, *Science* **314**, 1757 (2006).
7. M. König *et al.*, *Science* **318**, 766 (2007); published online 19 September 2007 (10.1126/science.1148047).
8. C. W. J. Beenakker, H. van Houten, *Solid State Phys.* **44**, 1 (1991).
9. M. Büttiker, *Phys. Rev. B* **38**, 9375 (1988).
10. M. Büttiker, *Phys. Rev. Lett.* **57**, 1761 (1986).
11. See supporting material on Science Online.
12. C. Brüne *et al.*, <http://arxiv.org/abs/0812.3768> (2008).
13. E. M. Hankiewicz, L. W. Molenkamp, T. Jungwirth, J. Sinova, *Phys. Rev. B* **70**, 241301(R) (2004).
14. We thank T. Beringer, N. Eikenberg, M. König, and S. Wiedmann for assistance in some of the experiments. Supported by Deutsche Forschungsgemeinschaft grant SFB 410; German-Israeli Foundation grant I-881-138.7/2005; NSF grant DMR-0342832; the Alexander von Humboldt Foundation; the U.S. Department of Energy, Office of Basic Energy Sciences, under contract DE-AC03-76SF00515; the Focus Center Research Program (FCRP) Center on Functional Engineered Nanoarchitectonics; the National Science and Engineering Research Council of Canada; and the Stanford Graduate Fellowship Program. Computational work was made possible by the facilities of the Shared Hierarchical Academic Research Computing Network ([www.sharcnet.ca](http://www.sharcnet.ca)).

#### Supporting Online Material

[www.sciencemag.org/cgi/content/full/325/5938/294/DC1](http://www.sciencemag.org/cgi/content/full/325/5938/294/DC1)  
SOM Text  
Figs. S1 to S9  
Table S1  
References

8 April 2009; accepted 11 June 2009  
10.1126/science.1174736

## REPORTS

# Higher-Order Photon Bunching in a Semiconductor Microcavity

M. Aßmann,<sup>1</sup> F. Veit,<sup>1</sup> M. Bayer,<sup>1\*</sup> M. van der Poel,<sup>2</sup> J. M. Hvam<sup>2</sup>

Quantum mechanically indistinguishable particles such as photons may show collective behavior. Therefore, an appropriate description of a light field must consider the properties of an assembly of photons instead of independent particles. We have studied multiphoton correlations up to fourth order in the single-mode emission of a semiconductor microcavity in the weak and strong coupling regimes. The counting statistics of single photons were recorded with picosecond time resolution, allowing quantitative measurement of the few-photon bunching inside light pulses. Our results show bunching behavior in the strong coupling case, which vanishes in the weak coupling regime as the cavity starts lasing. In particular, we verify the  $n$  factorial prediction for the zero-delay correlation function of  $n$  thermal light photons.

The discovery of two-photon bunching in thermal light by Hanbury Brown and Twiss (1) marked a turning point for the development of quantum optics (2) and has also found appli-

cations in a variety of fields, from particle physics (3) to ultracold quantum gases (4). Photon bunching is the tendency of indistinguishable photons, emitted by a thermal or chaotic light source, to show

an enhanced joint detection probability compared with statistically independent particles that are emitted, for instance, by lasers. The explanation of this bunching relies on quantum interference between indistinguishable  $n$  particle probability amplitudes leading to excess joint detections if the photon number follows the Bose-Einstein distribution (5, 6).

The quantity describing bunching for two photons is the second-order intensity correlation function defined as

$$g^{(2)}(t, \tau) = \frac{\langle \hat{n}(t) \hat{n}(t + \tau) \rangle}{\langle \hat{n}(t) \rangle \langle \hat{n}(t + \tau) \rangle} \quad (1)$$

where  $\hat{n} = \hat{a}^\dagger \hat{a}$  is the photon number operator,  $t$  and  $t + \tau$  are the detection times of the two

<sup>1</sup>Experimentelle Physik II, Technische Universität Dortmund, D-44221 Dortmund, Germany. <sup>2</sup>DTU Fotonik, Technical University of Denmark, DK-2800 Kongens Lyngby, Denmark.

\*To whom correspondence should be addressed: E-mail: [manfred.bayer@tu-dortmund.de](mailto:manfred.bayer@tu-dortmund.de)